COMPUTATIONAL INVESTIGATION INTO THE INFLUENCE OF YAW ON THE AERODYNAMICS OF AN ISOLATED WHEEL IN FREE AIR

T. D. Kothalawala, A. Gatto, L. Wrobel

Brunel University, UK

Abstract

This paper details a computational investigation into the influence of yaw angle on the near and far-field aerodynamics of an isolated wheel in free air. Unsteady Reynolds-Averaged Navier-Stokes was used as the primary analysis tool to analyse the complex flow features around this configuration, with principal vortical positions and magnitudes, overall lift, drag, and side force coefficients, as well as on-surface pressures characterised within the work presented. Fundamentally, the flow was found to be highly vortical in nature, particularly within the wake region of the wheel, with changes in yaw shown to have a significant impact on the surface flow, wake structure, as well as calculated force coefficients.

Keywords

Wheel Aerodynamics, landing gear, yawed bluff body aerodynamics

Introduction

Across the world every day, thousands of commercial aircraft flights take-off, travel to a destination, then land. During this landing phase, the aircraft is typically in a high lift condition with slats, flaps, and landing gear deployed and exposed to the oncoming airstream. In this configuration, the interaction of these systems with the outside airstream generates significant aerodynamic noise that causes serious psychological and physiological effects to millions of people who live in close proximity to these airports [Jones (2009), Knottnerus (2009), Schipper et al (2001)]. Within the European Union, Directive 2002/30/EC limits large commercial aircraft noise for approach with commitments within the EU to reduce noise levels by 10dB (EPNL) between 2000 and 2020. This remains a significant challenge, and with a 5dB reduction required just to accommodate an expected threefold expansion of air traffic by 2025 [Moss (2010)], ensures that efforts to reduce aircraft-related aerodynamic noise will continue well into the foreseeable future.

Over the last two decades, efforts within this area have focussed primarily on power plant and high-lift aerodynamic aeroacoustic emissions [Dobrzynski (2010), Azarpeyvand et al (2006), Lazos (2002), Lazos (2002b)], however, as these systems have been developed and improved, aircraft landing gear is now one of the most prominent sources of the total airframe noise on approach [Dobrzynski (2010)]. Unfortunately, the complexity of a modern aircraft landing gear is substantial, comprising several dissimilar bluff-body components operating, and interacting within, close proximity to one another which can make accurate analysis very difficult [Lazos (2002), Lazos (2002b)]. As a first logical step to enhance this fundamental understanding, work centred on the individual components such as the wheels themselves can provide a solid foundation for analysis of the combination. Unfortunately for aircraft landing gear, previous studies considering the aerodynamics of an isolated wheel in free-air are particularly scarce with investigators favouring the related flow case of an isolated wheel in contact with the ground which has particular relevance to automotive applications [Fackrell (1974), McManus and Zhang (2006), Fackrell and Harvey (1975), Stapleford and Carr (1970), Axon (1998), Wray (2003), Dimitriou and Klussmann

(2006)]. This gap in understanding represents a deficiency that needs to be addressed if the challenging goals set by regulatory authorities are to be met.

One of the most recent investigations into the aerodynamics of an isolated wheel in free air was conducted by Zhang et al (2013). This work used several experimental tools to identify various flow structures over two different wheel configurations. These structures included areas of flow separation and attachment around the wheel sides, hub detail, over the top and bottom of the wheel, as well as the generation of four distinct, asymmetrically positioned, streamwise trailing vortices, emanating and convecting downstream from the rear face of the wheel. Within the wake region, PIV results also showed a nearly symmetric, characteristic deficit in streamwise velocity magnitude representative of low flow velocity and relatively high surface pressure magnitudes (near C_p=0) compared to results over the top and bottom of the wheel (C_p= -1). Overall drag coefficients (un-tripped) were also measured with the wheel and supporting strut combination (C_D=0.24-0.3) for Reynolds numbers > $0.8x10^6$ with inferred isolated-wheel results (corrected for measurements from the support itself) yielding C_D≈0.19. The four distinct vortices observed are also in agreement with Cogotti's (1983) predicted theory of the formation of two pairs of counter-rotating vortices behind a stationary wheel in free air.

For direct consideration of the influence of yaw angle on the aerodynamics of an isolated wheel configuration in free-air (very low aspect ratio circular cylinders), there exists a limited body of work. This is particularly surprising due to the everyday engineering significance and widespread application of this particular flow case. Considering the influence of yaw angle (up to 60°) on large aspect ratio circular cylinders in free air initially, previous work has shown a dependence of increasing yaw angle to a reduction in the value of critical Reynolds number compared to the un-yawed case [Bursnall and Loftin (1951)]. This relationship becomes more complicated with aspect ratio reduction down to L/D=1, where the flow has demonstrated much more asymmetric three-dimensionality, with inherent dependencies on variables including free stream turbulence, edge profile, boundary layer condition and Reynolds number [Fackrell (1974), Bursnall and Loftin (1951), Zdravkovich (1989), Gerrard (1966)]. The similar case of discs and cylinders rotating in free air was also considered by Zdravkovich (2003) and Seifert (2012). Low aspect ratio cylinders rotating with a peripheral angular velocity equivalent to the free stream flow velocity show an immediate shift in wake structure distinctly different from the stationary case, with the ultimate production of a net lift force. For this case, flow separation is observed to move upstream on the side of the rotating cylinder that opposes the direction of the free stream flow, displacing the wake towards that side of the wheel. Conversely, on the side of the rotating cylinder co-inciding with the free stream flow direction flow separation is delayed(magnus effect).

For the related case of isolated wheels in contact with the ground, Wray (2003), Cogotti (1983) and Mears (2004) have all investigated the influence of yaw on the flow field aerodynamics. Wray (2003) conducted a computational study used the k-ε realizable turbulence model as well as the two models used in a similar computational study by Axon (1998). Results from this study indicated that this turbulence model was much better suited at predicting the wake structure and surface pressures of the isolated wheel with Cogotti (1983) and Mears (2004) showing also that both lift and drag peaked (and reduced thereafter) at 15° yaw. Mears (2004) investigated more moderate degrees of yaw up to 5° with results for drag showing an increase of 5% for 5° yaw with a lift reduction of 17% seemingly in direct conflict with the results of Cogotti (1983).

MacCarthy (2010) also investigated the influence of moderate yaw angles on the aerodynamics of an isolated wheel in contact with the ground. From this study, one of the main influences of yaw angle on the resulting downstream flow field and wake was the apparent 'skewing' of the entrained down-flow over the top of the wheel in the direction of yaw. The skewing of this dominant down-flow mechanism was also found to offset the positions and relative magnitudes of the generated, upper counter-rotating vortex pair of vortices, with the bias tending to favour the windward side of the model. Interestingly,

work within this study also included on the effects of exposed hub detail in non-yawed configurations showing that both an increase in overall lateral wake size, as well as drag coefficient, resulted from the exposed hub detail when compared to the hub cavities covered.

As an initial exploratory investigation and to supplement the available literature, the current work will focus on characterising the aerodynamics of an isolated wheel in free air in a yawed configuration. This condition is a common occurrence in every day aircraft landing gear operational flight and represents a fundamental initial investigation prior to the consideration of more complicated multiple-component combinations.

Computational Methodology

For this study, the isolated wheel configuration selected was the A2 wheel configuration experimentally tested in Fackrell (1974). The decision to choose this configuration as the basis for the analysis was driven by the need to provide a solid foundation of experimental and computational data for subsequent validation and verification of the computational methodology and subsequent flow field dynamics. This wheel geometry also contains both hub detail approximating a simplified typical landing gear hub configuration (albeit more asymmetric normally) as well as a tyre width to diameter ratio indicative of a landing gear wheel.

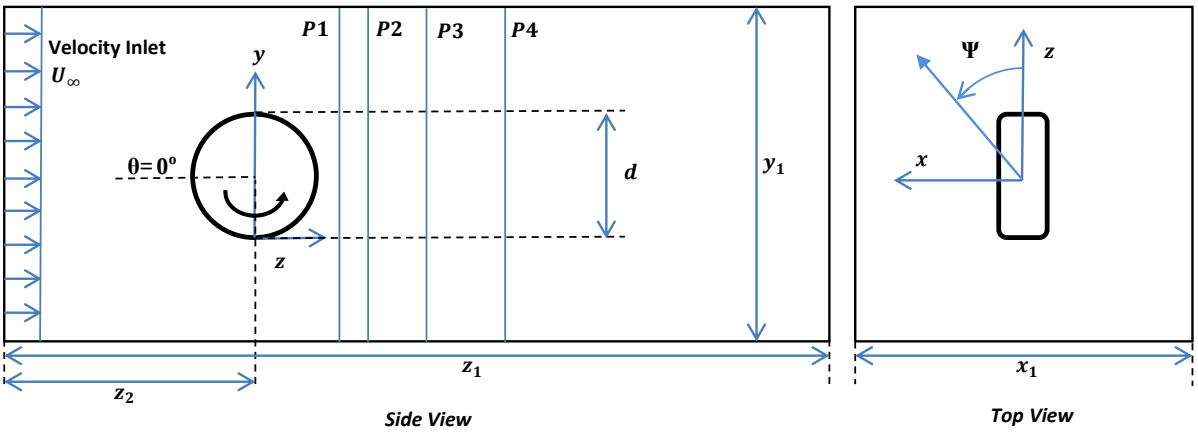

Figure 1. Computational Geometry

A schematic of the computational domain used is detailed in Figure 1. For all simulations, the wheel centre (width (l) and diameter (d) of 0.191m and 0.416m) was positioned at the geometric centre of the height and width of the domain, positioned at a distance z_2 downstream from the inlet plane. Positive yaw angle was applied to the wheel as defined in Figure 1. The final values selected for x_1, y_1, and z_1 as well as suitable grid density were chosen after a rigorous initial investigation involving both boundary and mesh refinement studies in which all of these variables were changed from a first initial estimate until results exhibited insensitivity with further modification. For this investigation, the scaling factors for boundary locations and grid density were applied through a course and fine configuration being half and double the sizes originally selected. On completion of this study, a final computational domain measuring z_1=24d in length, x_1= 4.4d in width, and y_1=6d in height, comprising 5 million structured-hexahedral cells, was selected as the baseline.

For all URANS computations, the k-ε realizable turbulence closure model was chosen. This model has been used in the past over similar bluff body configurations with generally acceptable correlation with experimental data and convergence capabilities [McManus and Zhang (2006)]. Boundary layer modelling was implemented through the use of the enhanced wall treatment due to the complex flow structures expected and the y+ value maintained at less than 2.5 over the entire wheel. The wheel (Figure 2) was modelled within the computational methodology as a smooth, no-slip wall so the

velocities on the wall can be set appropriately; in this case of a stationary wheel the wall velocity was set as zero. A velocity boundary inlet condition was used for all computations with the outlet domain modelled as a pressure outlet set to standard atmospheric conditions. Turbulence intensity for both the inlet and outlet domains was set to 0.2% with all four sides of the computational domain modelled as symmetry planes to negate the need to resolve wall boundary layers. To simulate the typical crosswind approach conditions of an aircraft, yaw angles of between ψ = 0-15° in steps of 5° were selected for analysis, with the yaw angle reference centre position located at the geometric centre of the wheel (y/d=0.5). For the grids incorporating wheel yaw, the near-field region of the baseline grid (ψ = 0°) was rotated by an angle about the +y axis representative of the yaw angle required. The far-field mesh was then constructed around these yawed near-field blocks to complete the computational domain (example shown in Figure 3). The Reynolds number (Re_n) based on wheel diameter, was $1.1x10^6$. The baseline computational domain comprised up to 140 structured blocks, positioned both within the near-field and far-field.

All results obtained from the URANS solver were obtained using a time increment of 0.00006s representing a non-dimensional time step of 0.0057 based on free stream velocity and wheel diameter. This time step was selected after initial investigations indicated that smaller time steps ($1x10^{-5}$s) had no appreciable influence on the final results obtained. For each time step, residuals were allowed to converge to a minimum standard of three orders of magnitude for 20 iterations per time step. Computational discretization was performed initially using first-order schemes for pressure, momentum and turbulence quantities to minimise computational expense before enacting second-order discretization schemes after an initial development period. After this initial first-order development period, the flow was allowed to further develop for an additional 17.3 non-dimensional time units before data sampling for mean flow statistics was initiated. Mean flow quantities were thereafter calculated after a subsequent 173 non-dimensional time units.

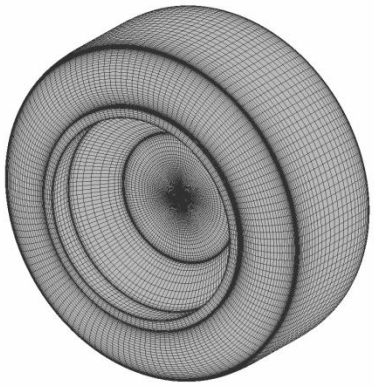

Figure 2.Wheel surface grid

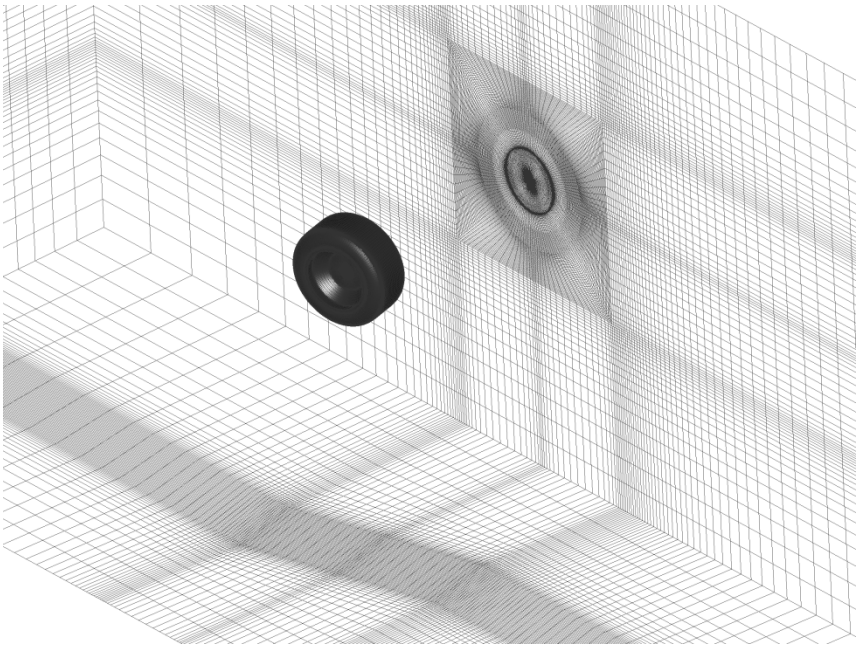

Figure 3. Computational grid with 15° yaw angle applied (flow direction from the left).

Experimental Validation of Computational Methodology

Before presentation and discussion of the results from the computational analysis, where available and appropriate, both experimental and computational results available in the current literature will be compared to the baseline case of the isolated, non-yawed, wheel in free-air to validate and verify the computational methodology. Where possible, this validation involves the use of both mean surface data as well as near-field wake data, however, particularly for the latter, limited data exists for comparison

As an initial comparison, Figure 4a shows the mean co-efficient of surface pressures along the wheel centreline (x/d=0) obtained from the current URANS study plotted against centreline experimental data manually extracted from literature [Zhang et al (2013), Lazos (2002)]. As can be seen in the figure, there is excellent agreement to Zhang et al (2013) over most of the wheel centreline circumference with maximum deviations found to be typically less than $\Delta C_P \approx 0.05$. The work from Zhang et al (2013) involved a dedicated experimental investigation of a similar-sized isolated wheel (with asymmetric hub detail) at a similar flow velocity. Agreement with Lazos (2002), which was extracted from the front wheel of a 4 wheel landing gear model, is much less correlated, but nevertheless, does show general qualitative agreement with that of the isolated wheel flow cases presented. For both comparisons, it is evident that the URANS solution tends to predict higher mean pressure coefficients within the wake region surrounding $\theta = 180°$ than those obtained experimentally. This trend has been identified in other studies comparing both URANS to higher-order computational methods as well as experimental studies [Hedges et al (2002)]. Comparing the data included from Lazos (2002), flow separation along the centreline tends to occur earlier ($\theta \approx 150°$ & 240°) with more asymmetric wake behaviour, indicating in agreement with [Lazos (2002), Lazos (2002b)], that influence of the subsequent rear wheel is significant on the aerodynamics of the front wheel of a landing gear. The presence of support struts/axles in Lazos (2002) would also complicate the wake characteristics for this configuration.

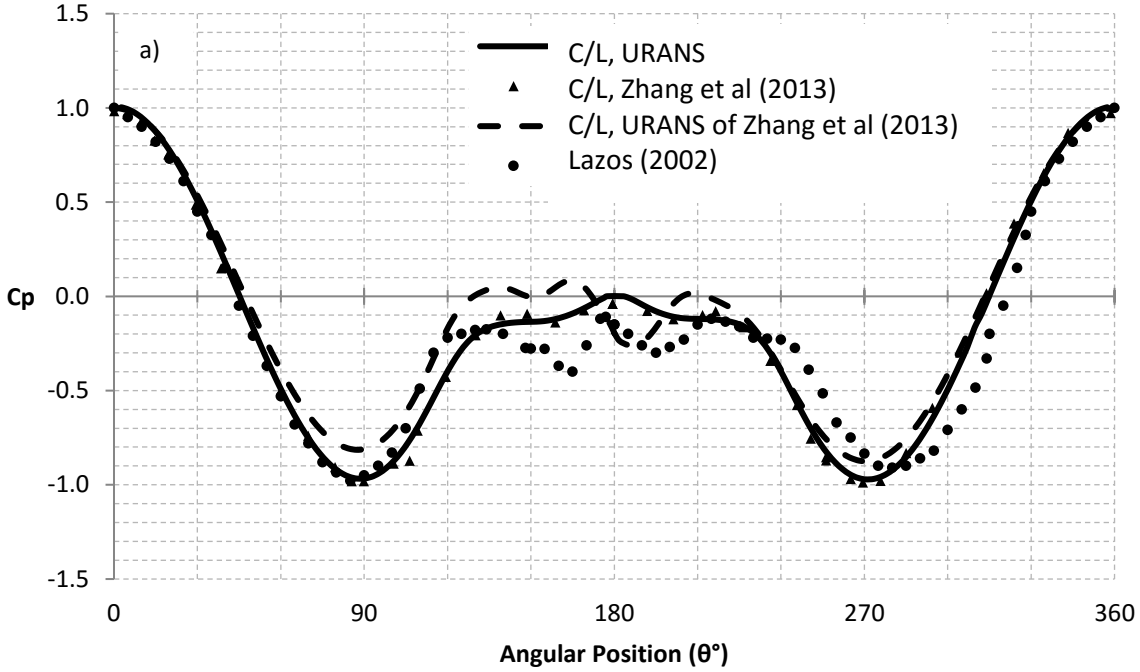

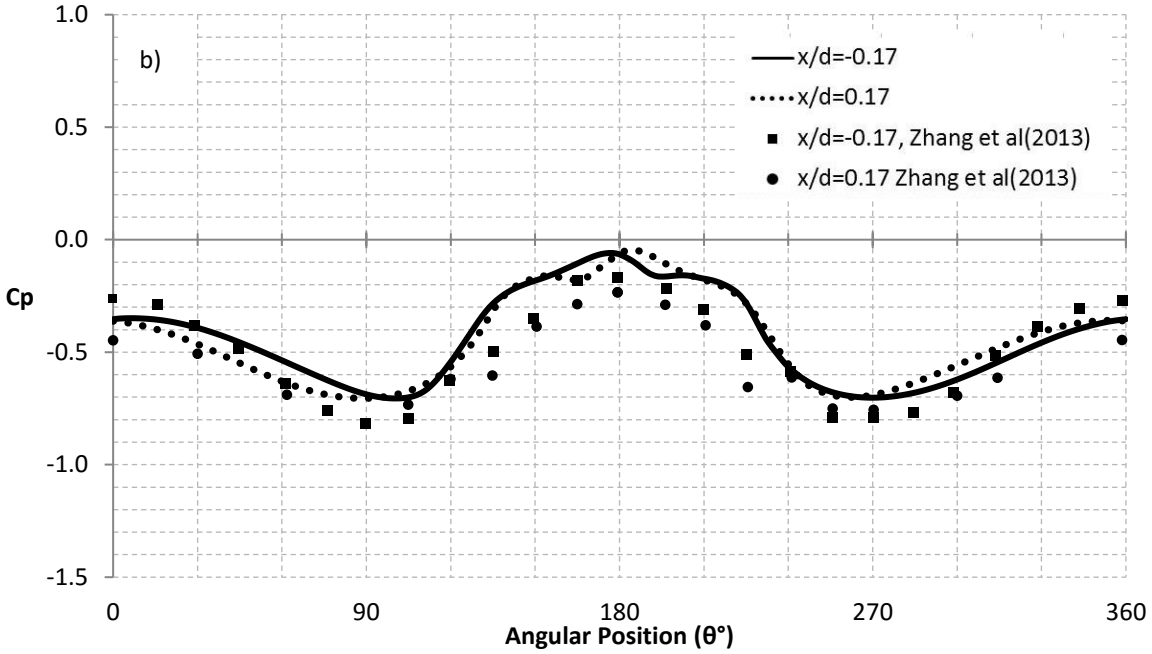

.

Figure 4. Comparison of mean pressure data conducted at Re_n =1.1 x10^6 with experimental work at Re_n=1.3x10^6 [Zhang et al (2013)] & Re_n = 6x10^5 [Lazos (2002)]: a) centreline, b) x/d=±0.17

The wheel geometry used for the experimental investigation by Zhang et al (2013) was also drawn on CAD software and simulated to validate the experimental findings and the computational methodology. The centreline surface pressure distribution for this case is also presented in Figure 4a and shows the general expected trend. However, discrepancies are present at the back of the wheel, but are suggested to be due to the unsteady nature of the wake region. Additionally, the general trend is over predicted, although this has previously been shown by Hedges et al (2002) to be a factor when

comparing URANS simulations to experimental results. Separation is observed at $\theta = 132°$ and $\theta = 209°$, showing agreement to the experimental study with variances of up to 13%.

Comparing experimental mean pressure coefficient data (Figure 4b) at x/d=±0.17 from the wheel centreline, results also show reasonably coherent correlation between the two sets of isolated wheel data. This is particularly evident in regions on the wheel where attached flow is expected ($\theta < 120°$ and ($\theta > 240°$) with agreement degrading in areas where more complicated flow physics and flow separation occurs ($150° < \theta < 220°$). Off-centreline surface pressure is known to be very sensitive to wheel profile [Fackrell (1974)] and from Figure 4, the qualitative differences evident, together with differences in hub detail, are thought to be the main factors responsible for the observed differences in the data.

Comparisons of mean drag coefficient between the two isolated wheel studies also show reasonably good agreement. Results of drag coefficient reported in Zhang et al (2013) for both the wheel and support sting without artificial boundary layer tripping ($Re_n > 1 \times 10^6$) were reported as $C_D \approx 0.29$-0.3. Overall drag coefficient for the present URANS study, modelling the wheel only, was measured at $C_D = 0.35$ ($Re_n = 1.1 \times 10^6$). If consideration is given to the influence of the sting drag supporting the wheel from Zhang et al (2013) whose individual drag was estimated at $C_D = 0.11$ (un-tripped), inferred overall wheel drag coefficient reduces to $C_D \approx 0.19$. It should be noted however, that in accounting for this difference, the A2 wheel profile used in the present study, has near-symmetric, wholly evacuated hub detail allowing the generation of further flow stagnation regions within the inside of the hub region. Allowing the flow to enter this region and stagnate would further increase the overall drag of the wheel with previous studies showing differences in exposed and covered hub detail representing as much as a further 27% increase in drag [Mercker and Berneburg (1992)]. Moreover, it should also be noted that the hub detail described in the experimental study [Zhang et al (2013)] on the 'boss' side has no perceivable evacuated area, exposing the flow field to a much more streamlined wheel side producing less internal stagnated regions of flow, and conceivably, less aerodynamic drag. This reasoning is also supported from estimates of individual wheel drag coefficients extracted from 'no hub' landing gear wheels ($C_D \approx 0.15$-0.16 [Hedges et al (2002)]). Inherently, these configurations are much more streamlined inhibiting free stream flow impingement onto downstream internal hub surfaces. Additionally, although URANS computations does show good agreement, this method was also observed to over-predict drag coefficients upto 9.7% when compared to experimental results modelling the turbulent flow past a cylinder when comparing experimental results to URANS, LES & DES methods, with the two latter methods showing better agreement to the experimental results with variances upto 1.2% [Benim et al. (2008), Benim et al. (2005). The computational study modelling the wheel used by Zhang et al (2013) provided a drag coefficient of $C_D = 0.26$, showing general agreement to the experimental study and good agreement with the present URANS study. Additionally, Fackrell (1974) stated that the A2 wheel configuration comprises of a drag contribution from the hub ($C_D = 0.08$), therefore deducting this from the present drag force in this study (to represent a streamlined hub configuration, similar to that used by Zhang et al (2013)) would yield a drag force of $C_D = 0.27$ showing good agreement to the experimental study by Zhang et al (2013) and to their geometry which was computationally modelled in this study.

Qualitative comparisons of the general wake dynamics observed from the current study also show general agreement to other published literature. Figure 5 provides baseline wake information representative of the centreline, non-dimensional, streamwise velocity at wheel mid-width and mid-height. Considering Figure 5a initially, the baseline wake characteristics are similar in general topology to that presented in the isolated wheel experimental investigation Zhang et al (2013) and the rear wheel wake characteristics of the 4-wheel complete landing gear study presented by Lazos (2002).

Characteristic of this wake are the contours of non-dimensional streamwise vorticity magnitude emanating from directly behind the wheel with very low flow velocity experienced at wheel mid-height. URANS results from the present study, calculated within the inner-most region of the wake were very close to zero with results observed in the literature [Lazos (2002), Zhang et al (2013)] reported with a similar magnitude both behind an isolated wheel and within the wake of the rear wheel of a 4-wheel landing gear [Lazos (2002)]. Contour plots of non-dimensional streamwise velocity at mid-height (y/d=0.5 – Figure 5b) also show general qualitative agreement with similar topology presented for both the 'simple' and 'complex' hub configurations presented in Zhang et al (2013). The simulated CFD results of the geometry used by Zhang et al (2013), illustrated Figure 5c and Figure 5d also show good agreement to the current study and the experimental results, showing regions of low velocity magnitude directly behind the wheel with similar wake shape and size. Evident in all of these comparative cases, are a pair of near symmetric regions of flow velocity behind the wheel.

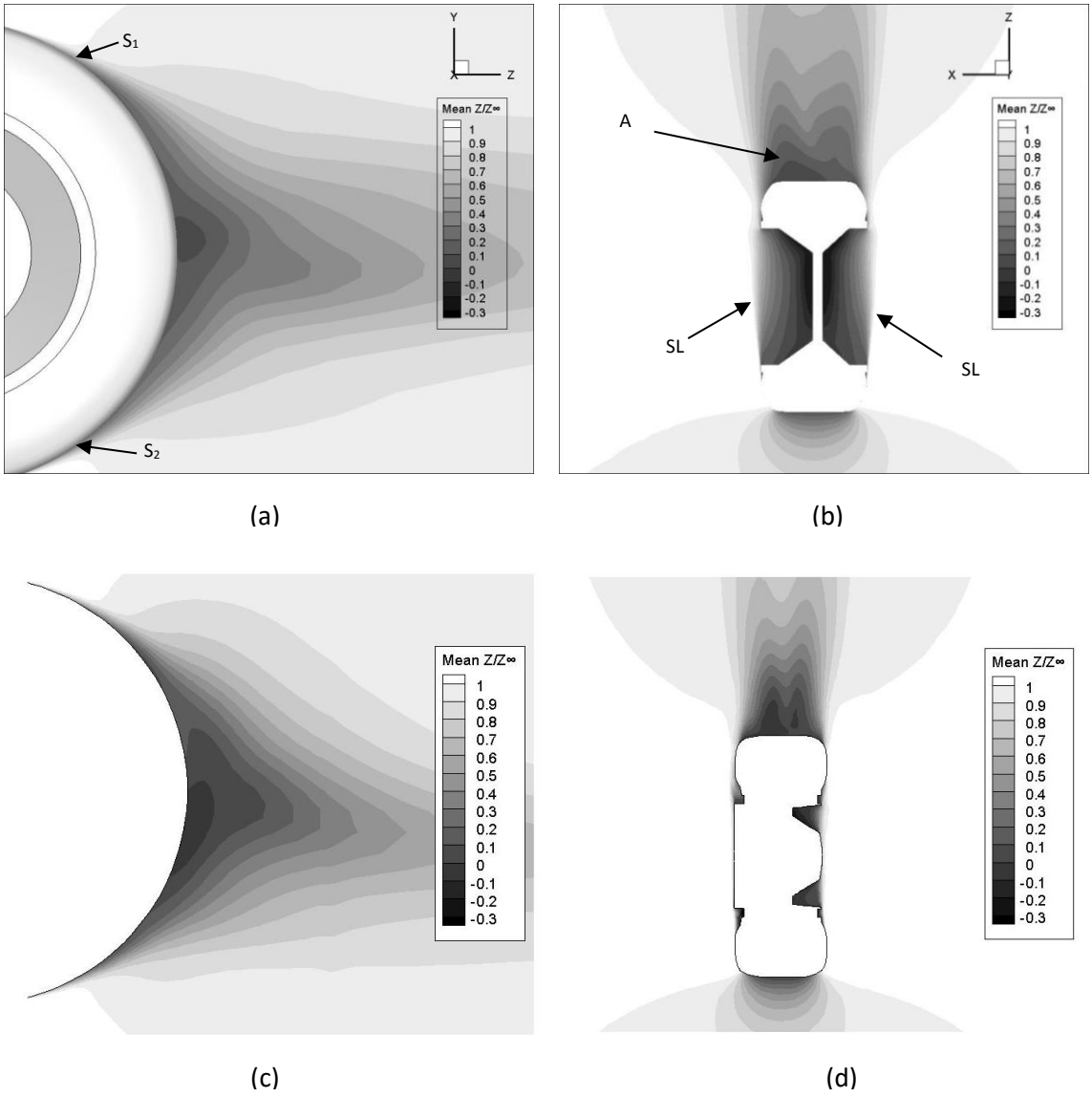

Figure 5. Contour plots of streamwise velocity; Current study: (a) x/d=0, (b) y/d=0.5 (Re_n =1.1 x10^6), CFD of Zhang et al (2013) wheel geometry: (c) x/d=0, (d) y/d=0.5 (Re_n =1.3 x10^6)

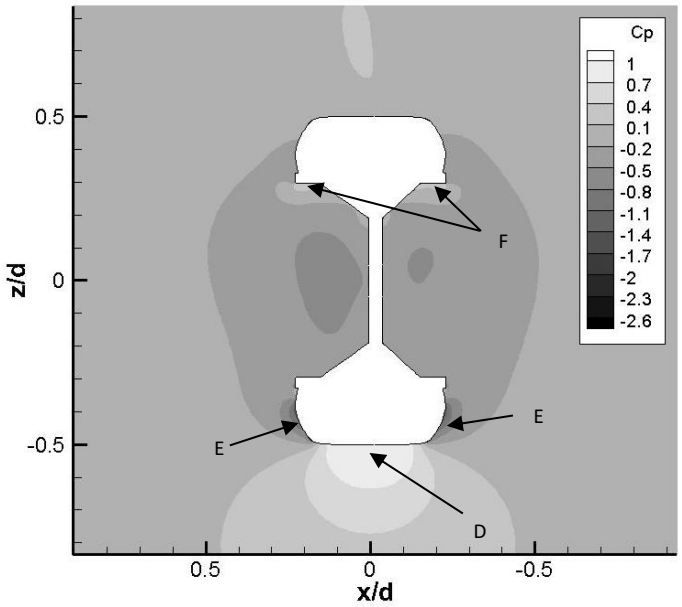

Figure 6. Contour plot of C_p at y/d=0.5 (Re_n =1.1 x10^6)

Results and Discussion

Baseline flow physics

In order to compare directly the influence of applied yaw angle on the flow physics on the isolated wheel aerodynamics, the fundamental flow physics dominating the baseline flow case of a non-yawed, free-air wheel, is first characterised. Presented in Figures 6 and 7 are the results obtained from the URANS simulations on this flow case including non-dimensional vorticity magnitude together with mean velocity direction and magnitude. To aid in interrogating and correlating the results from this flow case to current understanding, contours of mean surface pressure at the wheel mid-height (y/d=0.5) are shown in Figure 6. At this analysis plane (y/d=0.5) and discussed in conjunction with Figure 5a, there is a substantial region of stagnated air (D) located on the front of the wheel face. From this position, the flow accelerates around both the top and bottom of the wheel as well as around the sides, achieving a maximum mean suction pressure magnitude and ultimate separation angle (θ_s) of C_p = -0.14 at θ_s = 231° (S_1) on the top and C_p = -0.20 at θ_s = 145° on the bottom (S_2) of the wheel respectively. Prominent on both sides of the wheel adjacent to the front regions of flow stagnation, there is also evident a crescent shaped region of suction pressure (E) $C_p \approx$ -1.34 where the flow, upon being fully retarded by the front face of the wheel, accelerates around both sides of the wheel edge at this mid-plane (Figure 6), in agreement with Hedges et al (2002). Subsequent to these regions of flow acceleration, a separated shear layer forms over the wheel hubs (SL – Figure 5b) with the flow found to impinge onto the back inner face of the exposed, evacuated hub (indicated by F in Figure 6), reaching a mean pressure magnitude of C_p = 0.35. This is a near-symmetric characteristic over both sides of the wheel. The transfer of this flow momentum to the wheel through this physical mechanism is what would be expected to increase the drag over the more streamlined hub configurations discussed and compared earlier. After passing over the evacuated hub, the flow reattaches to the rear side edges before being entrained within the wake behind the wheel. The assemble-averaged coefficient of lift and drag coefficients for this flow case were found to be C_L=-0.01 and C_D=0.35 respectively.

Considering the vorticity plot shown in Figure 7, the wake physics seem to be dominated by a primary interaction of intense down-flow (B) from the top of the wheel, and originating from the wheel centreline (x/d=0), with intense up-flow (C) from the bottom of the wheel. In both cases, maximum mean flow velocity magnitude was found to be approximately symmetric. Results also indicate that as a consequence of these two distinct flows over the top and bottom of the wheel, and their interaction with the wheel side-flow, four distinct and separate vortices are created and convect downstream (Figure 7a). The physical mechanisms for the generation of these separate vortical structures are fundamental to the resulting flow field in several distinct ways [Axerio-Cilies et al (2012)]. As is shown in Figure 7a, the four vortices generated play a significant role in entraining the flow from the top and bottom of the wheel, whereby delaying flow separation and producing a much smaller wake size than would be experienced from larger aspect ratio configurations. This is a common characteristic of finite length bluff-bodies with high inherent vorticity and typically results in a drag reduction with decrease in aspect ratio.

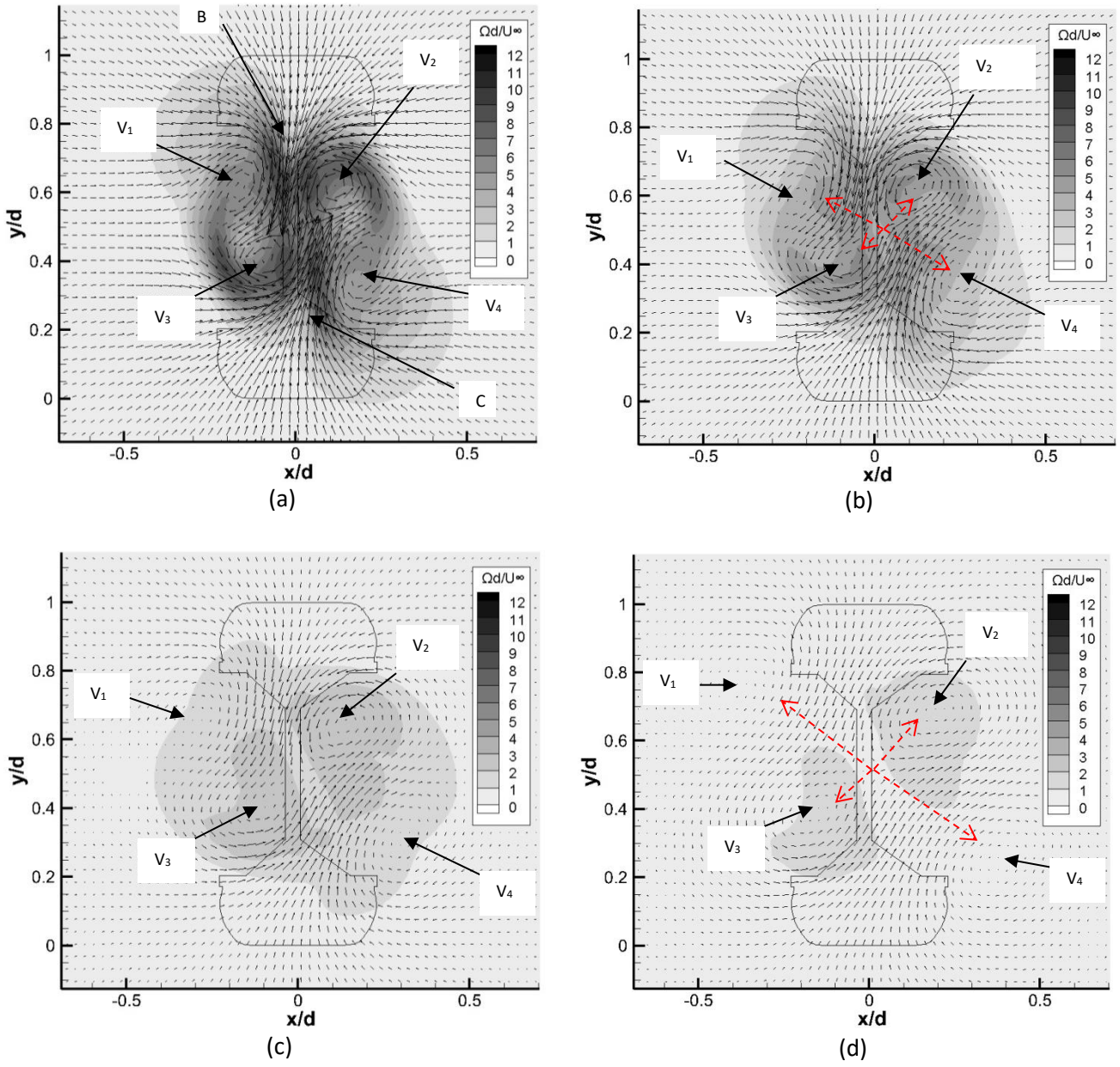

Figure 7, Non-dimensional vorticity plots for 0° yaw; a) z/d=0.75, b) z/d=1, c) z/d=1.5, d) z/d=2.5 (Re_n =1.1 x10^6)

Although significant, this entrainment mechanism still remains of insufficient intensity to remove the generation of a separated wake completely (full base pressure recovery), and as is evident in Figure 5a, there remains a region of very low velocity flow on the rear surface of the wheel defining a separated wake. Similar characteristics of the wake flow behind both isolated wheels in free air, as well as the rear wheels of complete landing gears, are detailed in Lazos (2002) and Zhang et al (2013). Another important characteristic of the vortices shown is they are generated as counter-rotating pairs, both within the top (V_1, V_2) and bottom halves (V_3, V_4) of the wheel wake.

For this particular flow case, results show that at this downstream location (z/d=0.75), the four vortices are positioned relative to the wheel centreline with asymmetric vorticity magnitude intensities. The two sets of vortices, upon being created, were also found to translate away from each other forming a wake with intense inherent vorticity. Vortices V_1 and V_2, generated initially from either side of the top half of the wheel are shown to propagate downstream with the intense entrained downwash (B) over the top of the wheel favouring a bias in vortical position towards the left of the wheel centreline. Conversely vortices V_3 and V_4, initially developed on either side of the bottom of the wheel, are entrained from the intense up-wash (C) towards vortical positions bias to the right side of the wheel centreline. From flow-field interrogation further downstream (b) (c) (d), the upper left vortex V_1 & the lower right vortex V_4 appear to dissipate in to the free stream quicker than vortices V_2 & V_3, with almost negligible vorticity magnitude $\Omega d/U_\infty \approx 0.5$ for V_1 and V_4 at z/d = 2.5. Considering vortex core vorticity magnitude at z/d = 0.75, Figure 7(a), V_2 & V_3 are stronger than V_1 & V_4 by up to 34%. The downwash (B) from the top of the wheel being skewed to the left in essence pushes vortex V_1 outwards and away from the wheel in the horizontal and vertical direction allowing more space on the upper right side for vortex V_2 to be entrained in to the gap. Similarly on the lower half of the wheel, vortex V_4 is also pushed outwards by the intense up-flow (C) from the bottom of the wheel as is skewed to the right, again with increasing skewness further downstream whilst V_3 is entrained in to the central region on the lower left side. Overall with further subsequent downstream propagation, the higher intensity of V_2 & V_3 keeps these two vortices entrained into and near to the central region of the wheel by the skewed downwash and up-wash respectively, whilst this downwash & up-wash simultaneously pushes vortex V_1 & V_4 further away from the wheel, as shown by the arrows in Figure 7(a).

The Influence of Yaw Angle

With the application of 5 degrees of yaw, both significant and subtle changes in the physics of the flow-field are immediately evident. From Figure 8, perhaps the most striking feature of the wake dynamics is that there is a clear bias and asymmetric distribution of vorticity favouring the windward side of the wheel. Both the development of vortex size and intensity are now substantially more pronounced on this side of the wheel with the displacement of the developed vortex centres translated to x/d = 0.118, y/d = 0.724 (V_2) and x/d = 0.188, y/d = 0.457 (V_4) respectively. Additionally, significant changes in the number of distinct vortical structures present, as well as vortex core central magnitudes, have occurred. No direct evidence of the development of V_1 and V_3, seen for the zero yaw case, is evident from the z/d=0.75 streamwise location for the 5° yaw case signifying that a fundamental shift in the distribution of wake vorticity to a dominate two-vortex wake has occurred. Together with this fundamental overall change in wake dynamics, the application of wheel yaw has also resulted in a characteristic change in the entrainment flow physics over both the top and bottom of the wheel. Outlined for the zero yaw flow case shown in Figure 7, the flow entrainment over the top (B) and bottom (C) of the wheel was seen to undergo an interaction that resulted in the downwash from the top, upon interacting with the up-flow from the bottom, displacing to the left and right of one

another prior to subsequent convection downstream. From Figure 8, the added vorticity generated from wheel yaw on the windward side of the wheel is shown to both intensify and fortify the skewness of the entrainment over the bottom of the wheel (C' relative to C) with the entrainment from the top of the wheel, previously moving towards the left of the wheel (B), now being straightened to move directly down the wheel centreline (B' relative to B). Effectively, it seems that applied wheel yaw, and the augmented vorticity produced bias towards the windward side of the model, results in a further intensification of the resulting sideways flow entrainment to augment wake bias towards the windward side of the wheel. The skewing of the wake towards the windward side was also found by MacCarthy (2010) who analysed the wheel at moderate yaw angles up to 6°.

Considering central core vorticity magnitude, the application of 5° wheel yaw has increased the core vorticity magnitude of $V_{4'}$, increasing from $\Omega d/U_\infty$ =4.96 in Figure 7a, to $\Omega d/U_\infty$ =8.60 in Figure 8a. Correspondingly, vortex core vorticity magnitude for $V_{2'}$ has remained relatively invariant with $\Omega d/U_\infty$ =6.77 ($\Omega d/U_\infty$ =6.59 from Figure 7a) suggesting that the application of yaw has an effect on increasing net core vorticity magnitude on the bottom half of the wheel wake dynamics more than the

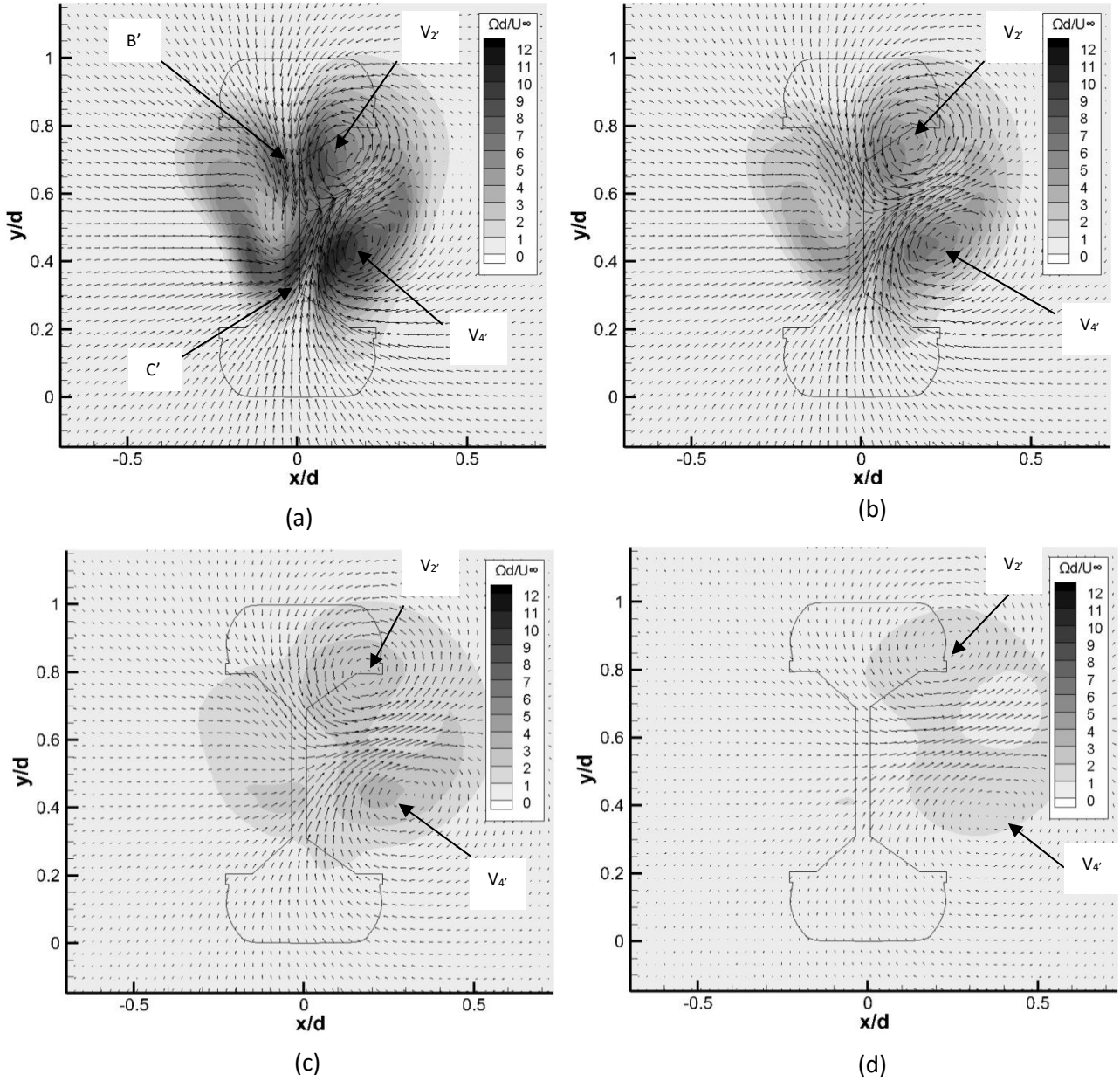

Figure 8. Non-dimensional vorticity plots for 5° yaw; a) z/d=0.75, b) z/d=1, c) z/d=1.5, d) z/d=2.5 (Re_n =1.1 x10^6)

top. It is also evident that through comparing Figures 7 and 8, that the application of a 5° yaw angle has increased the transverse displacement of the two primary vortex structures (V_2, V_4) with vortex core positions relative to Figure 7 being displaced by $\Delta x/d = 0.003$ and $\Delta x/d = 0.002$ for V_2 and V_4 respectively. For the 5 degree yaw case shown in Figure 8, there is also evident increased asymmetric transverse offset of vortex $V_{4'}$ relative to $V_{2'}$ most probably as a result of the more efficient constructive interference over the bottom of the wheel than over the top as discussed earlier for Figure 7. This difference, initially representing $\Delta x/d=0.07$ at $z/d=0.75$, was found to increase to $\Delta x/d=0.145$ at $z/d=2.5$. This tends to correspond to results obtained for the respective vortex core magnitudes with the bottom vortex (V_4) showing increased intensity over the one from the top (V_2). Additionally, and in similar trend to that found for the 0° yaw case, with subsequent propagation downstream from $z/d=0.75$, vortex core vorticity magnitudes for both $V_{2'}$ and V_4' were found to dissipate rapidly, with reductions of more than 80% from $z/d=0.75$ to $z/d=2.5$.

Comparing the results of mean pressure coefficient with 5° applied yaw shown in Figure 9 to the zero yaw case (Figure 6), overall, the surrounding pressure distribution shows an enhancement of suction pressure on the leeside of the model together with an overall increase in the pressure on the windward side. This is principally evident with the increase in the suction region around the front leeside edge of the wheel (E_1) to $C_p = -1.9$ from -1.34 at 0° yaw indicating increasing flow acceleration around the leeside front edge on the leeside of the wheel. This increase in suction pressure occurs in unison with a decrease in the suction pressure (E_2) on the windward side of the model ($C_p = -1.05$ from Figure 9 relative to $C_p = -1.34$ from Figure 6). This decrease is a result of relative exposure to the oncoming free stream. Together with the flow asymmetry found over the front edges of the wheel, there is also evident flow asymmetry within the flow stagnation regions impinging onto the rear face of the internal cavities of the wheel. Within these regions, there exists an increase in surface pressure within the windward side cavity that represents more than a 30% increase over the results found at zero yaw. Conversely, a similar decrease ($C_p = 0.26$ from Figure 9 relative to $C_p = 0.30$ from Figure 6) is shown within the leeside cavity illustrated for F_1. This would be expected as the leeside model cavity is now more shielded from direct exposure to the oncoming free stream.

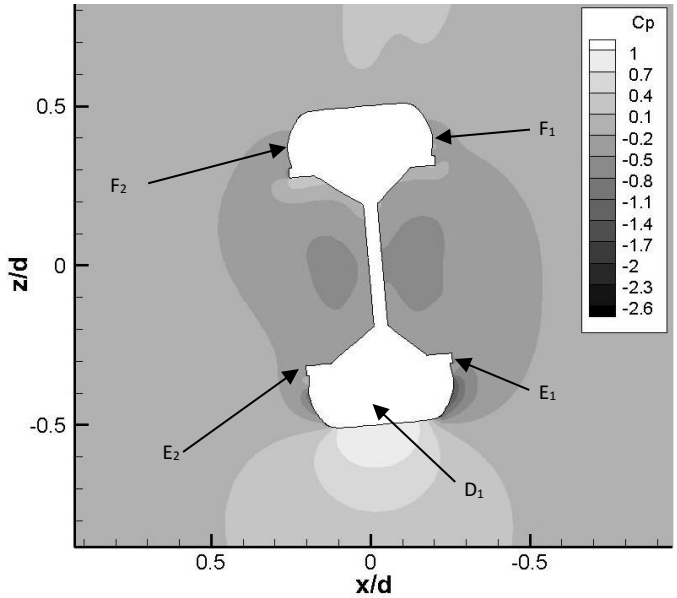

Figure 9. Contour plot of C_p at 5° yaw at y/d=0.5 (Re_n =1.1 x10^6)

With the application of a further change in yaw angle of 5 deg shown in Figure 10, the degree of flow asymmetry continues to increase as more of the windward side of the model becomes direclty exposed to the oncomming freestream. The suction region, indicated by E_3 in Figure 10. continues to support further flow acceleration around the leeside edge of the wheel with the maximum suction pressure magnitude of C_p = -2.60. This compares to the maximum suction pressures of C_p = -1.90 and C_p =-1.34 for 5° and 0° yaw respectively. Results from the corresponding internal cavity positions discussed earlier on this side of the wheel also exhibit a similar trend with results for positions F_3 and F_4 (Figure 10) giving results of C_p = 0.58 and C_p = 0.09 respectively. Also evident in the results with increasing applied yaw is the relative movement of the flow stagnation position across the front face of the wheel as yaw angle increases. From analysis of the results, this position of mean flow stagnation, which is located at the direct centre of the wheel front face for the 0° yaw case, translates with a bias towards the windward side of the model, by $\Delta x/d=0.04$ and $\Delta x/d=0.08$ for 5° and 10° yaw respectively representing an almost proportional linear displacement with applied yaw magnitude increase.

Comparing the wake dynamics of the effect of another 5° incremental increase in yaw angle to 10°, Figure 11 shows that the dominant two-vortex wake structure continues to persist from the case presented for 5°. With the additional increase in yaw angle applied to the wheel, the central core vortex magnitudes of V_2 and V_4 have continued to increase relative to the 5° case presented in Figure 9. Together with this increase in vorticity magnitudes, there is also an increase in the transverse displacement of the dominant pair of vortices towards the windward side of the wheel. Initially, at the spanwise location of z/d=0.75, this additional displacement caused through the additional increase in traverse flow entrainment is rather subtle being only marginally larger than that observed for the 5° yaw case outlined from Figure 8 as x/d=0.168 from Figure 11 and x/d=0.118 from Figure 8 for V_2, and x/d=0.222 from Figure 11 and x/d=0.188 from Figure 8, for V_4, however, with further propagation downstream the transverse displacement is seen to increase to x/d=0.356, y/d=0.822 for $V_{2''}$ and x/d=0.430, y/d=0.297 for $V_{4''}$, representing a marked increase over the 5 degree yaw. Also evident in the results from figure 11, is evidence that with the increase in yaw to 10 degree, the down-flow from over the top of the wheel and the up-flow from the bottom of the wheel has become markedly more symmetric under these flow conditions, with the strength of the vorticity, particularly over the top of the wheel (B), now strong enough to not only entrain the down-flow from the top of the wheel moving to the adjacent side of the up-flow (C) as evidenced earlier in Figure 7, but to now

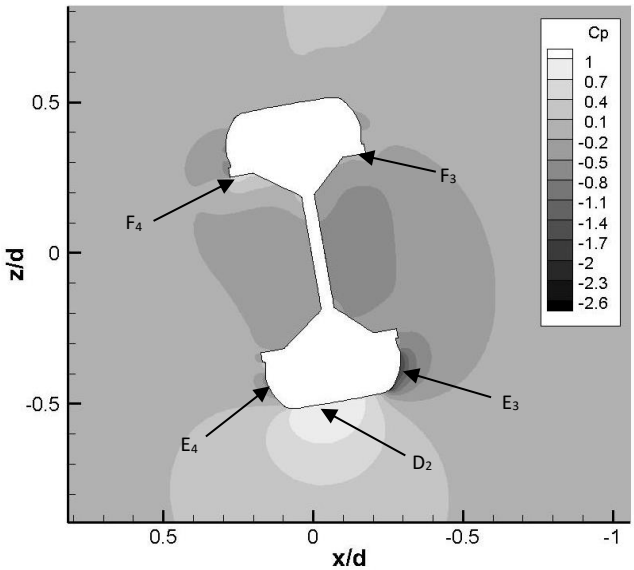

Figure 10. Contour plot of C_p at 10° yaw at y/d=0.5 (Re_n =1.1 x10^6)

fully entrain the flow towards the windward side of the wheel with a similar degree of intensity(B' relative to B").

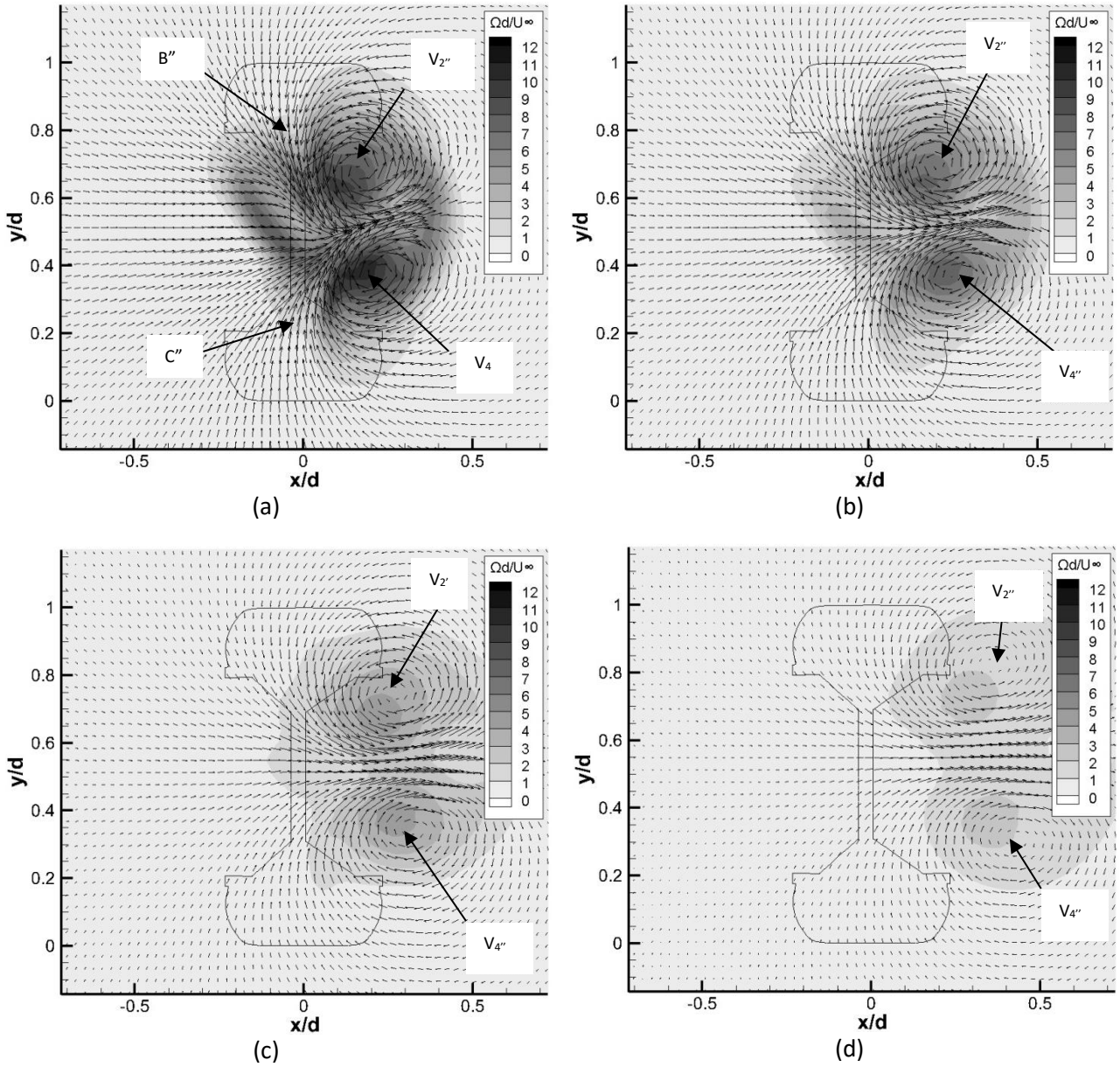

Figure 11. Non-dimensional vorticity plots for 10° yaw; a) z/d=0.75, b) z/d=1, c) z/d=1.5, d) z/d=2.5 (Re_n =1.1 x10^6)

With the application of 15 yaw, the wake dynamics continue to show the two-vortex dominant flow-field evident for both the 5° and 10° yaw cases. As is shown in figure 12, at x/d=0.75, the two intense and distinct vortical structures now possess nearly identical vorticity magnitudes ($\Omega d/U_\infty \approx 10$) each lying with near symmetry relative to the top and bottom halves of the developed wake. $V_{2'''}$, whose centre is positioned at x/d=0.248 and y/d=0.676, and generated from the intense shed vorticity from the free stream interaction with the rear half of the windward side of the model, is seen to propagate transversely to the right with intense entrainment of the central portion of the wake towards the direction of applied yaw angle (noted by A"' in Figure 12a). The magnitude of this intense cross flow entrainment for this analysis station, and generated as a consequence of the pair of counter-rotating vortices working in unison, was found to reach a peak cross flow magnitude of more than 70% of the

free stream. This percentage reduced to 32% at the furthest downstream analysis plane of z/d=2.5. Within the lower wake region, at z/d=2.5, V_4 showed highly symmetric characteristics when compared to the upper vortex position of V_2 within the developed wake with near identical displacements of $\Delta x/d \approx 0.28$ and $\Delta y/d \approx 0.105$ ($+\Delta y$ forV_2 and $-\Delta y$ for V_4) from z/d=0.75 to z/d=2.5. As with the results presented earlier, dissipation of vorticity within the central core regions with downstream propagation was also found to be substantial with a reduction of almost an order of magnitude with vortex propagation from z/d=0.75 to z/d=2.5.

Comparing the contour plots of pressure coefficient shown in Figure 13, the almost symmetric characteristics of the pressure field found in Figures 9 and 10 continue to be distorted towards a progressively higher asymmetric flow field with again substantial areas of significant localised low and high pressures experience over the wheel at mid-height. At this yaw configuration, the maximum stagnation pressure within the frontal region of the wheel continues to move away from the wheel centreline with the maximum stagnation pressure position now located at a position of $\Delta x/d = 0.11$ from the nominal wheel centreline. Either side of this position, the characteristics of the flow field mimic what has already been discussed in the earlier section at more moderate yaw angles, however the magnitudes of the regions of low pressure continue to increase. Within region E_5, the flow acceleration around the lee side of the front face of the wheel was found to reach a maximum suction pressure of $C_p = -3.0$ immediately adjacent to the wheel edge profile representing further increases of flow acceleration relative to the cases shown for 5° and 10° degrees of yaw. Additionally, the single dominant flow stagnation region evident on the windward rear face of the evacuated cavity was also found to increase in both size and magnitude under 15° yaw. At this location, C_p was found to be almost equivalent in magnitude to that observed at the front stagnation position with $C_p= 0.77$ (denoted at F_6).

Vortex Core Positions

To assess the overall influence of yaw angle on vortex core position, Figure 14 summarises the calculated relative displacement of the two dominant vortex structures (V_2, V_4) with downstream propagation referenced to z/d = 0.75($\Delta x/d=0$, $\Delta y/d=0$). Considering initially the transverse relative displacement ($\Delta x/d$), results show a clear trend to increasing relative traverse displacement to the windward side of the wheel with increasing degree of applied wheel yaw. Interestingly, while the upper vortex (V_2) moves with almost linear relative displacement with downstream propagation, the traverse displacement of V_4, exhibits some non-linear behaviour at lower yaw angles ($\psi<10°$). This result may be due to the asymmetric levels of constructive amplification discussed earlier resulting from the transverse flow physics (upper vortex – V_2) being unable to fully entrain the opposing wake flow from moving to the opposite leeside of the wheel (B relative to B' – Figures 7a and 8a). This does not occur for the bottom vortex, V_4, where this constructive amplification is free to occur. This effect was found to be most prominent at $\psi=5°$ for z/d=1 and z/d=2.5. These relatively significant and defined changes in transverse displacement with applied yaw were also found to occur with relatively small, but linear, changes in vertical displacement. As is shown from Figure 14b, the results exhibit both a relative insensitivity to applied yaw magnitude with very little defined trend or direct relationship relative to applied yaw angle.

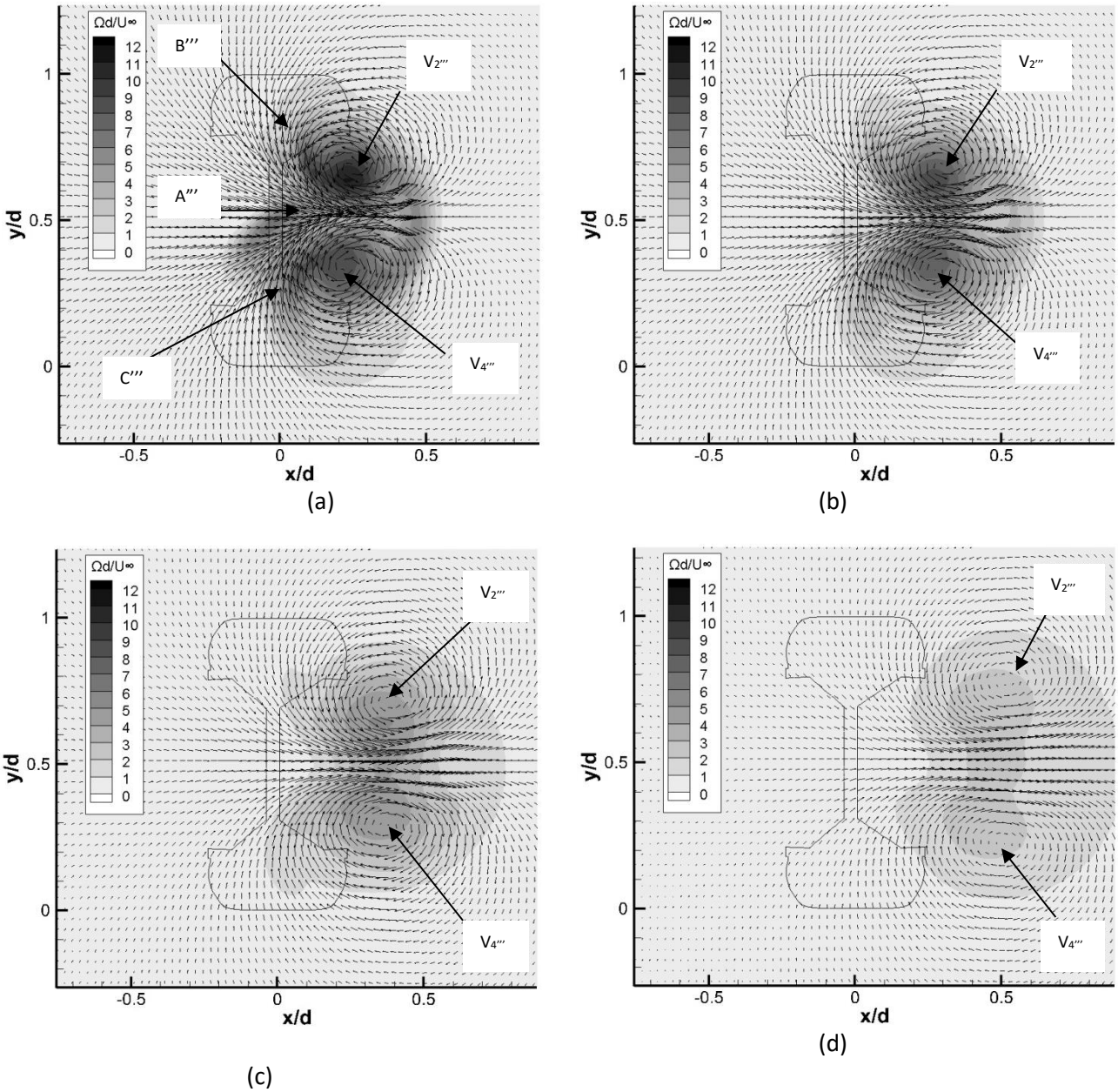

Figure 12, Non-dimensional vorticity plots for 15° yaw; a) z/d=0.75, b) z/d=1, c) z/d=1.5, d) z/d=2.5 (Re_n =1.1 x10^6)

Overall Lift, Drag, and Side Force coefficients

Table 1 outlines the overall lift, drag, and side force coefficients for the cases considered. As discussed earlier, the calculated drag coefficient for zero yaw when compared to the literature is higher at C_D = 0.35. As has already been discussed, this discrepancy is expected to result from the increased drag of the stagnated air impinging within the exposed hub cavities on the sides of the wheel. Mercker & Berneburg [25] indicated that up to a 27% increase in drag can occur with exposed hubs on a wheel in contact with the ground and this finding is in general agreement with the work carried in the present study. With the application of wheel yaw, results show that both drag and side force coefficients undergo a marked increase with the application up of 15° yaw. At this condition, the drag coefficient was calculated at C_D = 0.50. An increase in drag is expected with increasing yaw angle as MacCarthy (2010) found that the increase in lateral wake size due to the exposed hub would subsequently result in an increase in drag force. Side force coefficient showed an almost linear

increase up to a similar magnitude at ψ=15°, showing good agreement to the trend found by Cogotti (1983). As would be expected, the flow is reasonably symmetric over the top and bottom of the wheel, giving results for lift coefficient with little variation around a near-zero magnitude at both zero and non-zero yaw angles.

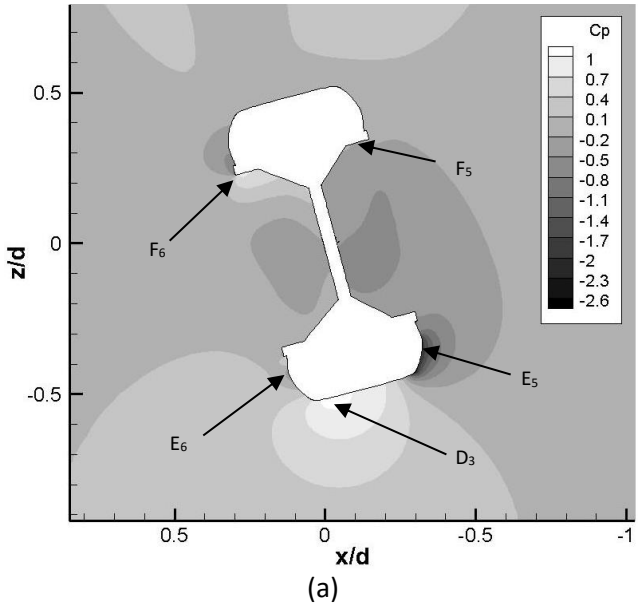

(a)

Figure 13. Contour plot of C_p at 15° yaw at y/d=0.5 (Re_n =1.1 x10^6)

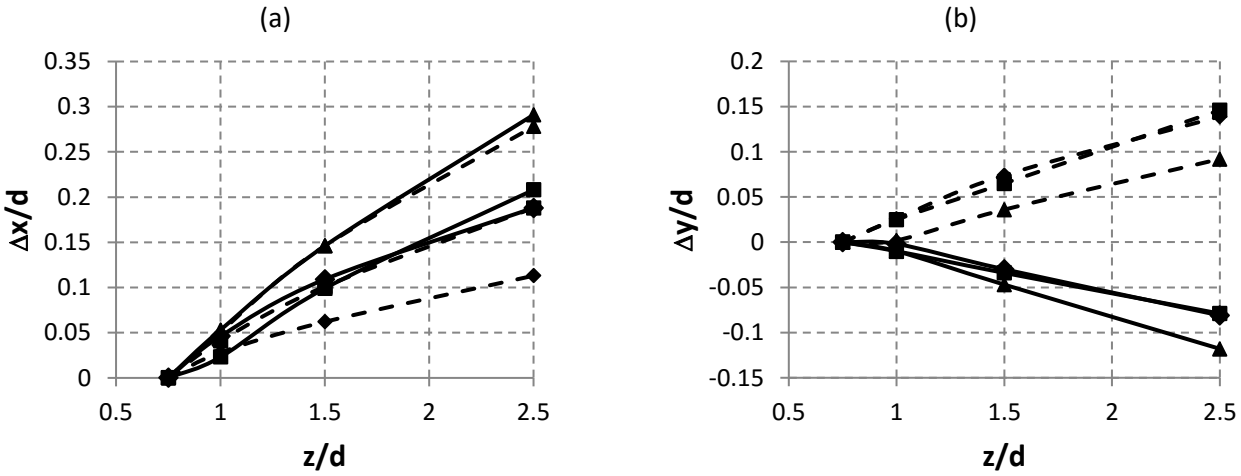

Figure 14. Vortex core displacements relative to z/d=0.75 with downstream propagation; V_2 (dashed), V_4 (solid) (Re_n =1.1 x10^6)

Force Coefficient	Wheel Yaw Angle			
	0°	**5°**	**10°**	**15°**
Lift	-0.01	-0.07	-0.04	0.02
Drag	0.35	0.35	0.39	0.50
Side	-0.05	-0.18	-0.35	-0.52

Table 1. Summary of lift, drag and side force coefficients for the yawed wheel (Re_n =1.1 x10^6)

Conclusion

An Unsteady Reynolds-Averaged Navier-Stokes investigation has been carried out into the effects of yaw angle of the free-air aerodynamics of an isolated wheel. Results obtained show that the flow field is highly vortical in nature with the wake physics detailing the development and entrainment of flow structures over the top, bottom, and sides of the wheel. At zero applied yaw angle, four distinct vortices are created and undergo relative movements within the wake that that are complex relative to the case of significant applied yaw. With the application of moderate yaw angle, the wake physics switches from a four vortex configuration to a dominant two-vortex configuration that persists with larger applied yaw angles up to 15°. Characteristic of the application of this level of applied yaw angle is the increase in transverse displacement of the vortex cores with propagation downstream. Significant increases in calculated drag coefficient and side force coefficient were also found with lift coefficient showing almost no change from a near-zero magnitude.

Future works to follow this current study involves focusing on the influence of rotation on a wheel with the combined effect of applied yaw angle. The current study essentially models a typical wheel of a landing gear with the presence of a cross-wind, represented by the yaw angle. However, the application of rotation will provide insight to the aerodynamic flow field around a wheel after take-off, with the subsequent application of yaw also representing the presence of a cross-wind. On completion of this work, comparisons can be made between 'in-contact with the ground' studies to identify key differences between the two configurations. Additionally, the effect of ground proximity with the effect of applied yaw and rotation would be of interest to understand how the flow-field dynamics change. The understanding of this influence would be beneficial as it represents a typical take-off and landing phase of an aircraft and could provide insight into how aircraft noise could be reduced in the future.

References

Jones, K., (2009) 'Aircraft Noise and Sleep Disturbance: A Review, Environmental Research and Consultancy Department', ERCD 0905.

Knottnerus, J. A., (2004) 'The Influence of Night-time Noise on Sleep and Health', Health Council of the Netherlands, publication no. 2004/14E.

Moss, J., (2010) 'The design of low-noise vehicles for air, road, and rail transportation' Noise/News International, Vol.18, No. 1, pp. 13-15.

Dobrzynski, W., (2010) 'Almost 40 years of airframe noise research: What did we achieve?', Journal of Aircraft, Vol 47, Issue 2, pp. 353-367.

Azarpeyvand, M., Self, R.H., and Golliard, J., (2006) 'Improved jet noise modelling using a new acoustic timescale', 12th AIAA/CEAS Aeroacoustics Conference, Cambridge, MA, AIAA-2006-2598, 8-10 May.

Lazos, B. S., (2002) 'Mean flow features around the inline wheels of four-wheel landing gear' Journal of Aircraft, Vol 40, No. 2, pp. 193-198.

Lazos, B. S., (2002b) Surface topology on the wheels of a generic four-wheel landing gear, J. Aircraft, 40(2), , pp. 2402-2411.

Fackrell J.E., (1974) 'The Aerodynamics of an Isolated Wheel Rotating in Contact with the Ground', Ph.D. thesis, University of London, U.K.

McManus, J. and Zhang, X., (2006) 'A Computational Study of the Flow Around an Isolated Wheel in Contact With Ground', Journal of Fluids Engineering, Vol. 128, Issue 3, pp. 520-530.

Fackrell, J. E., and Harvey, J. K., (1975) 'The Aerodynamics of an Isolated Road Wheel' AIAA Proceedings of the Second Symposium on Aerodynamics of Sports and Competition Automobiles, North Hollywood, CA,

Stapleford, W. R., and Carr, G. W., (1970) 'Aerodynamic Characteristics of Exposed Rotating Wheels', Technical Report 1970/2, Motor Industry Research Association.

Axon, L., (1998) 'The Aerodynamic Characteristics of Automobile Wheels – CFD Prediction and Wind Tunnel Experiment', Ph.D. Dissertation, College of Aeronautics, Cranfield University.

Wray, J., (2003) 'A CFD Analysis Into the Effect of Yaw Angle on the Flow Around an Isolated Rotating Wheel', MSc, Cranfield College of Aeronautics, Cranfield University.

Dimitriou, I., and Klussmann, S., (2006) 'Aerodynamic Forces of Exposed and Enclosed Rotating Wheels as an Example of the Synergy in the Development of Racing and Passenger Cars', 2006 SAE World Congress and Exhibition, 2006-01-0805.

Zhang X., Ma Z., Smith M. and Sanderson M., (2013) 'Aerodynamic and Acoustic Measurements of a Single Landing Gear Wheel', AIAA, 19th AIAA/CEAS Aeroacoustics Conference.

Bursnall, W. & Loftin, L. (1951) 'Experimental investigation of the pressure distribution about a yawed circular cylinder in the critical Reynolds number range', National Advisory Committee for Aeronautics Technical Note 2463.

Zdravkovich, M. M., Brand, V. P., Mathew, G., and Weston, A., (1989) 'Flow past short circular cylinders with two free ends', Journal of Fluid Mechanics, Vol. 203, pp. 557-575.

Gerrard, J. (1966) 'The three-dimensional structure of the wake of a circular cylinder', Journal of Fluid Mechanics, Vol. 25, pp. 143-164.

Cogotti, A. (1983) 'Aerodynamic Characteristics of Car Wheels', International Journal of Vehicle Design, Special Publication SP3, pp. 173-196.

Mears, A. P. (2004) 'The Aerodynamic Characteristics of an Exposed Racing Car Wheel', Ph. D. thesis, University of Durham.

MacCarthy, N. H., (2010) 'An Experimental Study of the Aerodynamics of Exposed Wheels', Ph.D., Department of Aeronautics, Imperial College.

Hedges, L. S., Travin, A. K., and Spalart, P. R., (2002) 'Detached-eddy simulations over a simplified landing gear', Journal of Fluids Engineering, Vol. 124, pp. 413-423.

Axerio-Cilies, J., Issakhanian, E., Jimenez, J., and Iaccarino, G., (2012) 'An Aerodynamic Investigation of an isolated Stationary Formula 1 Wheel Assembly', ASME Journal of Fluids Engineering, Vol. 134, pp. 021101.

Mercker, E. & Berneburg, H. (1992) 'On the simulation of road driving of a passenger car in a wind tunnel using a moving belt and rotating wheels', 3rd International Conference of Innovation and Reliability, Florence, April 8-10.

Benim, A. C., Nahavandi, A., & Syed, K. J. (2005). 'URANS and LES analysis of Turbulent Swirling Flows', *Progress in Computational Fluid Dynamics, 5*(8), 444-454.

Benim, A. C., Pasqualotto, E., & Suh, S. H. (2008). 'Modelling Turbulent Flow past a Circular Cylinder by RANS, URANS, LES and DES', *Progress in Computational Fluid Dynamics, 8*(5), 299-307

Schipper, Y., Nijkamp, P. and Rietveld, P. (2001) 'Aircraft noise valuation studies and meta-analysis', *Int. J. Environmental Technology and Management*, Vol. 1, No. 3, pp.317-320.

Zdravkovich, M. M. (2003) 'Flow Around Circular Cylinders', Oxford University Press

Seifert, J. (2012) 'A Review of the Magnus Effect in Aeronautics', ***Progress in Aerospace Sciences.***